Hepatitis B Virus Core Protein Domains Essential for Viral Capsid Assembly in a Cellular Context

Virgile Rat, Xavier Pinson, Florian Seigneuret, Stéphanie Durand, Charline Herrscher, Roxane Lemoine, Julien Burlaud-Gaillard, Pierre-Yvan Raynal, Christophe Hourioux, Philippe Roingeard, et al.

Hepatitis B virus core protein domains essential for viral capsid assembly in a cellular context

Authors: [1]Virgile Rat#, [5]Xavier Pinson#, [1]Florian Seigneuret#, [1]Stéphanie Durand, [1]Charline Herrscher, [3]Roxane Lemoine, [2]Julien Burlaud-Gaillard, [2]Pierre-Yvan Raynal, [1, 2]Christophe Hourioux, [1, 2]Philippe Roingeard, [4, 5]Marc Tramier* and [1]Hugues de Rocquigny**

[1] INSERM U1259 MAVIVH, Université de Tours and CHRU de Tours, 10 boulevard Tonnellé - BP 3223 37032 Tours Cedex 1 – France.

[2] Plate-Forme IBiSA des Microscopies, PPF ASB, Université de Tours and CHRU de Tours, 10 boulevard Tonnellé - BP 3223 37032 Tours Cedex 1 – France.

[3] Plateforme B Cell Ressources, EA4245 "Transplantation, Immunologie et Inflammation", Université de Tours, 10 Boulevard Tonnellé, 37032 Tours Cedex 1 – France.

[4] Univ Rennes, IGDR (Institute of Genetics and Development of Rennes) – UMR CNRS 6290, 2 Avenue du Professeur Léon Bernard, 35000 Rennes, F-35000, France.

[5] Microscopy Rennes Imaging Centre, SFR Biosit, UMS CNRS 3480- US INSERM 018, Université de Rennes, 2 Avenue du Professeur Léon Bernard, 35000 Rennes, France.

E-mail address of each author:

virgile.rat@etu.univ-tours.fr; xavier.pinson@univ-rennes1.fr; florian.seigneuret@univ-tours.fr; stephanie.durand@etu.univ-tours.fr; charline.herrscher@etu.univ-tours.fr; rlemoine@univ-tours.fr; julien.gaillard@univ-tours.fr ; raynal@univ-tours.fr ; christophe.hourioux@univ-tours.fr; philippe.roingeard@univ-tours.fr marc.tramier@univ-rennes1.fr; hderocquigny@univ-tours.fr

 # contributed equally to this work.

*** Corresponding author:**

Hugues de Rocquigny

Tel: 33 (2) 47 36 60 93 Fax : 33 (2) 47 36 61 26

e-mail: hderocquigny@univ-tours.fr

****Co-corresponding author:**

Marc Tramier

Tel: +33 (0)2 23 23 54 87 Fax : +33 (0)2 23 23 44 78

e-mail: marc.tramier@univ-rennes1.fr

Abstract:

Hepatitis B virus (HBV) core protein (HBc) is essential to the formation of the HBV capsid. HBc contains two domains: the N-terminal domain (NTD) corresponding to residues 1-140 essential to form the icosahedral shell and the C-terminal domain (CTD) corresponding to a basic and phosphorylated peptide, and required for DNA replication. The role of these two domains for HBV capsid assembly was essentially studied *in vitro* with HBc purified from mammalian or non-mammalian cell lysates but their respective role in living cells remains to be clarified. We therefore investigated the assembly of the HBV capsid in Huh7 cells, by combining FLIM (Fluorescence Lifetime Imaging Microscopy)/FRET (Förster's Resonance Energy Transfer), FCS (Fluorescence Correlation Spectroscopy) and TEM (Transmission Electron Microscopy) approaches. We found that wild-type HBc forms oligomers early after transfection and at a sub-micromolar concentration. These oligomers are homogeneously diffused throughout the cell. We quantified a stoichiometry ranging from ~170 to ~230 HBc proteins per oligomer, consistent with the visualization of eGFP-containing HBV capsid

shaped as native capsid particles by TEM. In contrast, no assembly was observed when HBc-NTD was expressed. This highlights the essential role of the CTD to form capsid in mammalian cells. Deletion of either the third helix or of the 124-135 residues of HBc had a dramatic impact on the assembly of the HBV capsid, inducing the formation of mis-assembled oligomers and monomers, respectively. This study shows that our approach using fluorescent derivatives of HBc is an innovative method to investigate HBV capsid formation.

Graphical abstract

Highlights:

. FLIM-FRET and FCS are suitable approaches to monitor HBV capsid assembly in the cytoplasm and in the nucleus.

. Wild type HBV capsid assembles early after the expression of the core protein, with a sub micromolar apparent Kd.

. TEM shows that chimeric HBc with an eGFP inserted in the protruding spicule can form capsid particles in mammalian cells.

. HBc-NTD does not form capsids when expressed in Huh7 cells.

. The deletion of the third α helix gives rise to a non-canonical capsid oligomerization, while the removal of the (124-135) domain inhibits HBc oligomerization.

Keywords

HBV, capsid, HBc, Assembly, FRET-FLIM, TEM

Abbreviations:

HBV: Hepatitis B virus; HBc: Hepatitis B core; FRET: Fluorescence Resonance Energy Transfer; FLIM: Fluorescence Lifetime Imaging Microscopy; TEM: Transmission Electron Microscopy

Introduction

There are approximately 250 million people chronically infected with the hepatitis B virus (HBV) worldwide and among them nearly 900,000 die annually, primarily as a result of clinical complications such as cirrhosis and hepatocellular carcinoma [1]. HBV is a 42 nm diameter hepatotropic DNA virus, with an outer envelope made by lipid-embedded small (S), middle (M) and large (L) surface proteins sheltering a 30 nm diameter icosahedral capsid [2]. This capsid corresponds to the oligomerisation of the core protein (HBc) and it is filled with a partially double stranded DNA referred to as 'relaxed circular' DNA (rcDNA), originating from the reverse transcription of the pre-genomic RNA (pgRNA) [3, 4]. In addition to these so called DANE particles [5], various studies have shown that the secreted particles have a differential composition. They correspond either to subviral particles made only of envelope proteins, to empty particles or to particles containing pgRNA [6-8].

HBV capsid shell was studied using different production sources to demonstrate that HBc is sufficient for capsid assembly (Table 1). HBc contains 183 residues and is composed of two major domains (Fig.1 A). The N terminal domain (NTD) is constituted by residues 1-140, and is essential for the self-assembly of the particle *in vitro* (for a review see [3]) (Table 1). The CTD (residues 149-183) contains a series of four ariginine rich domains (ARD) and all the seven potent phosphoacceptor sites that are both essential for pgRNA encapsidation and DNA synthesis [9-13]. This domain was originally localized in the internal layer of the capsid, but it can also protrude at the surface. Its presence at the surface was shown to depend on the presence or the absence of RNA or DNA, and on its phosphorylation status [14-19]. Lastly,

HBc contains a small and flexible spacer peptide (141-149), tethering the NTD and CTD domains and possibly regulating capsid assembly [20, 21].

In addition to the formation of the capsid, a significant number of studies indicate that HBc has pleiotropic functions in HBV cycle. These functions include nucleic acid (NA) chaperone activity during reverse transcription [12, 22], nuclear import of the genome [23] and the interaction with the covalently closed circular cccDNA[4]. Thus, the HBc protein represents a critical factor in virus replication, and a prominent target in developing strategies for new anti-viral molecules [24].

Details on the NTD structure were obtained by X-Ray at a resolution of 3.3Å [25], and by cryoEM [26-29]. More recently, the structure of HBc was entirely solved by cryoEM at a 2.6 to 2.8 Å-resolution, and it showed that the structure of the NTD domain remains largely unchanged in the entire protein [19]. It forms icosahedral shells either containing 120 HBc dimers (T=4 particles, 95%), or 90 HBc dimers (T=3 particles, 5%), arranged in both cases with quasi-equivalence [29]. For T=4, four similar conformations yield two conformers of HBc dimers, each one forming the characteristic four-helix bundles that appear as spikes on the surface of the capsid [13, 25, 30]. This four-helix bundle corresponds to the association of two α helices (H3 and H4) of each monomer. This interaction is mainly stabilized by an extensive amount of contacts between the H3 residues. These dimers are assembled in capsids via the multiple interactions of residues located in the fifth helical structure, the proline rich loop (128-136), and the C terminal arm [25].

The data pointing out the essential role of NTD in the formation of a capsid morphologically similar to capsids formed by a full length HBc were carried out *in vitro*, using approaches as high salt concentration and proteins purified from *E coli* (Table 1) [3, 29, 31]. Nevertheless, the NTD alone failed to assemble properly when purified from rabbit reticulocyte lysates suggesting that the CTD was also required [32]. Thus, the purpose of our study was to

visualize the assembly of the HBV capsid in more relevant cells, and in physiological conditions. We therefore imaged HBc capsid assembly over time by combining Fluorescence Lifetime Imaging Microscopy– Fluorescence Resonance Energy Transfer (FLIM-FRET), Fluorescent Correlation Spectroscopy (FCS), and by Transmission Electron Microscopy (TEM). These techniques were performed on human hepatoma cell lines Huh7 permissive for HBV replication [33] and transiently transfected by plasmid expressing HBc, together with HBc derivatives harbouring a fluorescent reporter at position 79-81 (Fig. 1A) [34-36]. FLIM-FRET and FCS analyses revealed that HBc/HBc-eGFP together with HBc-mCherry formed oligomers homogeneously distributed in the cell. Brightness analyses allowed to calculate the stoichiometry of HBc in oligomers and an apparent Kd. Using electron microscopy, we observed that these oligomers corresponded to capsid particles. We next used these approaches to detail which HBc sub domains are required for its assembly in mammalian cell context. We discovered that HBc-NTD fails to self-assemble, suggesting that the CTD is essential for the formation of wild-type capsids in a mammalian cell context. The third helix found essential for monomer-monomer interaction was removed in HBcΔαH3 and this deletion gave rise to monomeric HBc or misassembled aggregates. At least, the ^{124}VWIRTPPAYRPP^{135} sequence required for dimer oligomerisation was deleted and HBcΔ124-135 proteins were found diffusing mainly as monomers. Together, our results show that our microscopy methods can be used to track the assembly of the HBV capsid in a cellular context. This opens the way to the possibility of following the assembly of the HBV capsid during the replication cycle, and the effect of assembly inhibitors such as Capsid Assembly Modulator (CAMs) on the viral capsid structure.

Results

Rational design of HBc and HBc fluorescent proteins to monitor HBc oligomerization.

Figure 1

In order to study HBc oligomerisation by quantitative fluorescent microscopy, we designed HBc proteins fused to eGFP and mCherry. To this end, several strategies have already been described [37, 38], and the insertion of antigens in the c/e1 epitope was shown to poorly impact the capsid formation [39, 40]. Indeed, an eGFP protein (or a monomeric mCherry) flanked by glycine-rich linkers was inserted between residues 78 and 80 of HBc and electron microscopy revealed the formation of capsid-like particles of HBc149-eGFP, with surface-exposed eGFP domains [34, 36, 41, 42].

The plasmids encoding unlabelled and labelled HBc were constructed as described in the materials and methods section. Western blot analyses of HBc, HBc-eGFP and HBc-mCherry using an anti-HBc antibody revealed the expression of each protein at the expected molecular weight (Fig. 1B, panel 1). Next, we constructed plasmids coding for proteins deleted either from residues 51-71 and encompassing the third helix (HBcΔαH3), or from ^{124}VWIRTPPAYRPP^{135} (HBcΔ124-135) [25]. We then analyzed the expression of HBcΔαH3 (Fig. 1B, panel 3) and HBcΔ124 -135 (Fig. 1B, panel 4) and their respective fluorescent counterparts, and found that these proteins localized at their expected molecular weights. However, an additional band was observed for all mCherry derivatives, potentially suggesting a partial hydrolysis of these chimeric proteins.

Using the same strategy, we constructed plasmids expressing HBc-NTD, HBc-NTD-eGFP and HBc-NTD-mCherry. The two fluorescent proteins were detected at their expected molecular weights using an anti-HBc antibody (Fig. 1B, panel 2), in contrast to non-fluorescent NTD that was undetectable by western blot and by immunofluorescence (data not shown) and in agreement with recent reports [43, 44]. Given that the anti-HBc antibody

detected HBc-NTD-eGFP (Fig. 1B), we hypothesized that the insertion of a sequence in the c/e1 epitope could stabilize HBc-NTD. Hence, a HA/Flag tag was inserted in the apical loop of HBc, allowing the detection of HBc-NTD-HA/Flag with an anti-HA antibody (Fig.1B). We now refer to HBc-NTD-HA/Flag as HBc-NTD for the rest of the manuscript.

Co-localisation between HBc (or HBc derivatives) with their fluorescent counterpart

Figure 2

To verify the influence of eGFP on the cellular distribution of HBc and HBc derivatives Huh7 cells were first transiently transfected for 24h with a plasmid expressing unlabelled HBc or truncated HBc proteins. After fixation, cells were incubated with a human anti-HBc antibody, then with a fluorescent anti-human antibody coupled to Alexa 585 and finally observed by confocal microscopy (Fig. 2, upper panels).Wild type HBc and truncated HBc were diffusing the all cell and predominantly in the nucleus for HBc, HBc-ΔαH3 and HBc-Δ124-135 (Fig. 2 a-d), in agreement with the localization of HBc when it is expressed alone [45, 46]. We next transfected Huh7 cells with a combination of plasmids expressing unlabelled and eGFP-labelled HBc derivatives (Fig. 2, lower panels). This combination of plasmids contained 0.7 µg of plasmid coding for unlabeled HBc and 0.3 µg of plasmid coding for eGFP-labelled HBc, to attenuate the impact of eGFP on HBc assembly according to a previously-reported strategy [37, 47, 48]. Nuclei were stained with DAPI, and proteins were localized through the eGFP fluorescence. As shown in the lower panels of figure 2, cells that expressed HBc with HBc-eGFP, and all HBc derivatives together with their fluorescent counterparts accumulated predominantly in the nucleus, along with a diffused fluorescence in the cytoplasm. Note that the distribution of HBc-eGFP (Fig. 2e) was in contrast with the pattern observed in an earlier report using an assembly-incompetent fluorescent HBc with a tandem-repeat of eGFP at the N terminus of core protein [37]. All together, these results

show that the cellular localization of HBc or HBc truncated proteins is similar with or without eGFP, suggesting the limited impact of eGFP on the cellular distribution of HBc.

Imaging HBc oligomerization monitored by FLIM in cells.

Figure 3 and 4

To follow HBc oligomerisation, we used the FLIM method to monitor FRET between eGFP and mCherry-labelled HBc [49]. These two fluorescent proteins are commonly used as a donor/acceptor pair to monitor protein/protein interactions by FLIM-based FRET (for review see [50, 51]). The donor eGFP has a high quantum yield (0.8) and a mono-exponential time resolved fluorescence decay [52]. The acceptor mCherry has an absorption spectrum that overlaps the fluorescence spectrum of eGFP, giving a large Förster R_0 distance (where the transfer efficiency is 50%) of about 54 Å [53]. In FLIM-based FRET, the donor lifetime varies based on the surrounding nanoenvironment, and it can be measured pixel per pixel. The presence of an acceptor in the immediate vicinity of the donor fluorophore allows a transfer of energy between donor and acceptor, shortening the fluorescence lifetime of the donor eGFP. The FLIM technique determines the fluorescence lifetime (τ) of the donor and τ values can be imaged using a pseudocolor scale.

First, Huh7 cells were transfected with a plasmid expressing eGFP or the tandem eGFP-mCherry, and analyzed 24h post transfection. The use of a fluorescent tandem was used to estimate the FRET efficiency in this cellular model. The fluorescence lifetime of eGFP was 2.5±0.01 ns while the fluorescence lifetime of eGFP tethered to mCherry dropped to 2.23±0.04 ns. Using Equation (1) described in the materials and methods section, this drop in τ corresponded to a FRET efficiency of 11.7±2 %, in agreement with an earlier report [54]. FLIM images were built using an arbitrary color scale ranging from 1 ns (orange) to 2.6 ns (red). Cells expressing eGFP (τ = 2.5±0.01 ns) appeared then in blue (Fig. 3, image a), and

cells expressing the eGFP-mCherry tandem (τ = 2.23±0.04 ns) appeared in red (Fig. 3, image b). The color was homogeneously distributed throughout the cell, in agreement with the diffused localization of these reporter proteins [55]. FLIM analyses of cells expressing eGFP and eGFP-mCherry was also carried out at 48 et 72h post transfection, without significant modifications of eGFP τ (data not shown).

We next calculated the fluorescence lifetime of eGFP fused to HBc in cells transfected by a combination of plasmids expressing HBc/HBc-eGFP (ratio 0.7/0.3) at 24h post transfection. When compared to eGFP alone, eGFP lifetime was lowered in the presence of HBc (2.06±0.04 ns) (Fig. 3c). Image rendering of this drop corresponded to a pseudocolored dark blue cell (compare Fig. 3a and 3c), showing that eGFP lifetime was modified by its fusion to the HBc protein. This control was also performed at 48h and 72h, without any significant modification in the lifetime of HBc-eGFP at this timepoints (data not shown). HBc-eGFP lifetime values at 48h and 72h were used to calculate the FRET efficiency as function of time post transfection (Fig. 4). Compared to eGFP alone, the shorter lifetime of eGFP when fused to HBc could originate from a misfolded eGFP protein. This was further suggested by the twofold decrease of the extinction coefficient calculated on Core 1-149 containing an internal eGFP [34].

Then, cells transfected by a mixture of plasmids expressing HBc/HBc-eGFP/HBc-mCherry (ratio 0.7/0.1/0.2) were imaged at 24h, 48h and 72h post transfection to monitor HBc oligomerisation in function of time. At 24h post transfection, the eGFP mean lifetime dropped to 1.51±0.03 ns and remained stable over time (1.46±0.04 ns at 48h, and 1.41±0.05 ns at 72h) giving rise to cells pseudocolored yellow (Fig. 3, images d, e, and f). Using the equation 1, we calculated an average FRET efficiency of 28 to 30% at 24, 48 and 72h (Fig. 4, yellow rectangles). This strong FRET efficiency showed that HBc molecules are closely packed, allowing a close proximity between the eGFP and mCherry tags. The absence of FRET

variation in function of time suggested that HBc oligomers were probably formed along or just after the translation process.

The impact of the HBc C-terminus domain on the assembly of HBc was assessed using the same strategy. As mentioned above, the absence of unlabelled HBc-NTD expression [43] prompted us to analyze cells expressing a mixture of HBc-NTD containing an HA/Flag tags together with the HBc-NTD-eGFP and HBc-NTD-mCherry counterparts. In cells expressing HBc-NTD/HBc-NTD-eGFP (ratio 0.7/0.3), the eGFP mean lifetime was of 2.14 ± 0.01ns (Fig. 3, image g), and the co-expression of these proteins with HBc-NTD-mCherry gave a mean τ equal to 2.05±0.03 ns. Consistent with this slight decrease of τ, cells were pseudocolored in dark blue (Fig. 3, image h). This weak variation of lifetime was not dependent on the time of protein expression, as the eGFP mean lifetime calculated at 48h and 72h post transfection were of 2.03±0.04 ns and 2.12±0.05 ns respectively, thus leading to cells pseudocolored in light blue (Fig. 3, images i and j) and a FRET efficiency of ~3-5% (Fig. 4, dark blue boxes). This low FRET efficiency indicated that HBc-NTD proteins weakly condense, but they could diffuse as monomers/dimers in Huh7 cells. Alternatively, they could oligomerise in a non-canonical pseudo-capsid shell, avoiding the close proximity between the two fluorescent reporters.

We then investigated the role of HBc structure on the oligomerization of the protein. Helix 3 was described as a long helical hairpin involved in the dimerization of each HBc monomer, and with the (124-135) stretch consisting on the bottom of the fifth helix and the following proline-rich sequence in interaction between dimer subunits [25]. Deletion of the third helix showed a heterogenous decrease of the mean lifetime at 24h post transfection (1.85±0.15 ns) with two populations of cells, pseudocolored blue (not shown) and green (Fig. 3, image l). This heterogeneity of τ was translated in a large FRET distribution ranging from 0 to a FRET similar to the wild-type FRET level (Fig. 4, green box). Interestingly, HBc-ΔαH3-eGFP

lifetime decreased to 1.5±0.14 ns as function of time post transfection, leading to cells pseudocolored orange/yellow (Fig. 3, images m and n). After 72h post transfection, τ was not statistically different from the lifetime obtained with wild-type HBc (Fig. 4, green bars). These results indicated a compaction of HBc-ΔαH3 oligomers with time, and/or an increase in the oligomer size so that the number of acceptor molecules in close proximity of each donor molecule would increases.

The deletion of (124-135) peptide had a more profound effect on HBc oligomerisation since τ remained stable at 2-2.1 ns, leading to cells pseudocolored blue (Fig. 3p). In contrast to HBc-ΔαH3, the time of protein expression up to 72h had only a slight effect on HBc-Δ(124-135)-eGFP lifetime with apparition of cells pseudocolored light blue (Fig. 3, images q and r) without a clear increase of the FRET mean efficiency (Fig. 4, light blue boxes).

Taken together, our data indicate that HBc forms oligomers in the cytoplasm and the nucleus. The homogeneous spatio-temporal distribution of τ suggests that HBc oligomerisation is neither restricted to a specific cytoplasmic domain nor to the time of expression (i.e. protein concentration). This oligomerisation requires both the C terminus and the (124-135) sequence, while the kinetics of HBc oligomerization depends on the third helix.

HBc oligomerization monitored by Photo Counting Histogram (PCH) analysis

Figure 5

To further characterize the oligomerization of HBc, FCS was performed on cell expressing HBc or HBc derivatives together with their fluorescent counterparts. This technique relies on the measurments of the intensity fluctuations of fluorescent species within a femtoliter volume to determine their physical parameters - diffusion time, local concentration, molecular brightness, which are related to their hydrodynamic and photophysical properties [56].

Fluorescence fluctuation measurements of eGFP fluorescence were acquired in the confocal volume during 30 seconds in live cells expressing HBc, HBc-NTD, HBcΔαH3 or HBcΔ124-135, together with their fluorescent counterparts. As mentioned for FLIM, the ratio of unlabeled to labelled plasmid was 0.7/0.3 to avoid the steric hindrance of the labelled eGFP during the core particle formation. Representative time traces of the photon counts were presented in Fig. 5A-D for each condition. Measurements with wild-type HBc showed fluctuations with a much larger amplitude relative to the mean than with the HBc-NTD or the HBcΔ124-135 proteins (compare upper panels of Fig. 5A with Fig. 5B and 5D). This was in agreement with the expected presence for HBc of oligomers as bigger and brighter particles going in and out the confocal volume, and causing larger fluctuations. In the case of HBcΔαH3, two different fluctuations were observed, potentially indicating the presence of either oligomers or monomers (Fig. 5C). A conventional autocorrelation curve obtained after the temporal auto-convolution of this time trace was also presented with a typical single species Brownian motion fit. Independently of the different measurements, fits of the autocorrelation curves always exhibited a single species model. This was also true for potentially mixed populations of monomers and oligomers (see Fig. 5C). The approach using autocorrelation analyses thus presented contrasted results with fluorescent proteins either diffusing with a fast residence time (around 300µs, Fig. 5 B, C and D) - characteristic of what was found for the monomeric eGFP expressed in live cells [57] - , or diffusing with a residence time more than 10-time longer (around 10 ms, Fig. 5 A and C) - representative of eGFP oligomerized into a constituted core oligomer. With this analytic approach, we did not succeed in characterizing a mixed population with a double species model after fitting. This is directly related to the way of HBc forms particles, with a potential mixture of fast diffusing monomers having the single eGFP brightness and of slow diffusing oligomers, and with eGFP more than ten-fold brighter.

To finely analyze the formation of core particle oligomers from monomers, we decided to turn to the Photon Counting Histogram method (PCH) [58]. PCH gives access to the brightness of a fluorescent species and the number of fluorescent particles in the detection volume. In contrast with conventional autocorrelation that distinguish species with different diffusion times, the PCH approach allows to distinguish species of different brightness value. Thus, it is a very powerful method when the molecular mixture to analyze is constituted of species with different brightness. Experimental PCH curves were directly obtained from the time trace and plotted in Fig. 5A to D (red curves). Contrary to the autocorrelation curves, the analysis of these PCH curves allowed to distinguish monomers from oligomers, thereby opening up the possibility of quantifying the ratio between monomers and oligomers in the living cell. All FCS measurements (3 measurements per cell, n = 86 – 105 for each condition) were analyzed by PCH with a two species model: the monomeric species (freely diffusing HBc monomer) with a fixed brightness value q1 (the brightness obtained with a control measurement on cells expressing monomeric eGFP) and n1, which is the mean number of monomers diffusing in the observation volume. Accordingly, the oligomeric species were given a brightness value q2 and n2 being the mean number of oligomers diffusing in the observation volume. For some analyzed PCH, n2 was found close or equal to zero, which corresponds to the absence of oligomeric particles. For each cell analyzed, we then determined if oligomers were present ($n2 \neq 0$) or absent ($n2 = 0$). Fig. 5E represents the percentage of measurements where the oligomers were present for each condition. When measurements were performed in cells expressing wild-type HBc, oligomers were found in 83% of the cases. On the contrary, the presence of oligomers in cells expressing HBc-NTD or HBcΔ124-135 was found in 15% and 9.2% of the cases respectively. An intermediate situation was observed for HBcΔαH3, where oligomers were found present in 25.7% of measurements.

When oligomers were present, we are able to determine the size of these oligomeric particles through the quantification of their brightness. We calculated the number of labelled eGFP proteins in the oligomer by calculating the q2/q1 ratio (see Material and Methods for details) (Fig. 5F). For wild type HBc, the median value was 26.4, meaning that the brightness of an assembled core particle is 26.4 times the brightness of monomers (Fig. 5F). The brightness of the larger species is thus 25-30 times that of the smaller one, assuming that the smaller species is a single-labeled dimer HBc/HBc-eGFP. Previous studies showed that in HBc-NTD-eGFP capsids only about 40-50% of the labelled proteins were fluorescent, thus this brightness should correspond to about 50-70 HBc-eGFP [34]. Further considering the excess of unlabeled to labeled protein resulting from the plasmid ratio (0.7/0.3) used for transfection, the larger species should correspond to an oligomer of 170-230 copies of HBc. This experimental value is in the range of the 180 to 240 copies of HBc protein for T=4 or T=3 triangular organizations [28]. Interestingly, the median value for HBcΔαH3 was similar to the value obtained for HBc (Fig. 5F) showing that the HBcΔαH3 oligomers present in 25.7% of the measurements (Fig. 5E) contained the same range of fluorescent proteins as the wild type. In contrast, for both HBc-NTD and HBcΔ124-135, the median value of q2/q1 ratio was 6.2 and 6.3, respectively. In the few measurements where oligomers were observed (Fig. 5E), this demonstrates that both mutants generally originated smaller oligomers.

It is believed that HBc first dimerizes, and then it assembles in capsid in the cytoplasm (ref). Unfortunately, with our experimental setup we were not able to determine if the non-oligomeric form of HBc would be monomeric or dimeric. Indeed, our experimental procedure was to transfect 30% of labeled HBc with 70% of unlabeled ones. If dimers are formed, a large majority would have single-labeled eGFP, indistinguishable from monomers as all exhibited the same brightness.

We finaly used the brightness to measure protein binding curve inside the living cell. To this end, we plotted the percentage of eGFP molecules in assembled particles (eq. 2) as a function of the total concentration of eGFP-fused proteins expressed in the measured cell (eq.3) (Fig 5G). For cells expressing wild-type HBc (Fig. 5G; yellow dots), most of the measurements showed that this protein was essentially in an oligomeric form, and this even at low protein concentrations. The amount of wild type HBc for which 50% of the eGFP species were engaged in oligomers was about 0.7-0.8 µM, suggesting that the HBc capsid assembly was obtained at a sub-micromolar concentration. Conversely, in the case of cells expressing HBc-NTD or HBcΔ124-135 (Fig. 5G, blue and grey dots respectively), the vast majority of measurements showed the presence of the sole monomeric species, showing that these HBc mutants did not form oligomers. Consistent with the results shown on Fig 5E and 5F, HBcΔαH3 (Fig.5G, orange dots) displayed an intermediate situation, with measurements reflecting the presence of both monomeric and oligomeric species, suggesting that this protein retains the ability to form assembled particles at higher proteins concentrations.

Taken together, our FCS data are consistent with our FLIM-FRET experiments. On one hand, high FRET efficiencies obtained for HBc and HBcΔαH3 correspond to the formation of larger oligomers. On the other hand, the low FRET efficiencies obtained for HBc-NTD and HBcΔ124-135 corresponds to the formation of monomers or smaller oligomers. Moreover, we determined that a sub-micro molar concentration of wild-type core protein was sufficient for capsid assembly in living cells. Last, brightness measurements indicate that the larger HBc oligomers are capsid-sized.

Organization of HBc aggregates in cellular context viewed by immuno-electron microscopy

Figure 6

We then sought to determine if the mixture of HBc or HBc derivatives with their fluorescent counterparts were oligomerized in wild-type capsid particles. Cells were transfected with a plasmid expressing HBc together with a plasmid expressing HBc-eGFP (ratio 0.7/0.3), consistently with the conditions used for FLIM-FRET and FCS. After 24h of protein expression, cells were sorted by FACS and pellets were processed for immuno-TEM with a primary anti-eGFP antibody. In cells expressing HBc/HBc-eGFP, we observed 10 nm-gold beads – corresponding to the secondary antibody - surrounding a small, spherical and electron dense material (yellow arrows) and its size corresponded to the dimensions of a native capsid (Fig. 6a, enlargements and Fig. S1). The distance between the central core and the gold beads corresponded to the dimensions of the primary-secondary antibody pair. These findings indicate that eGFP-labelled HBc was incorporated in HBV capsids in cells. Conversely, cells expressing either HBc–NTD (Fig. 6b) or HBcΔ124-135 (Fig. 6d) showed gold beads dispersed throughout the cell, without a notable accumulation into clusters. Finally, regarding the deletion of the third helix with HBc-ΔαH3, we observed clusters of gold beads without the presence of a dense central core (Fig. 6c). Since Fig. 3 and 4 showed an increased FRET efficiency as a function of time post transfection for this construct, immuno-TEM was repeated at 72h. However, we did not observe the formation of capsids at this time point (data not shown). Overall, these results provide evidence that only eGFP-labelled HBc forms native-like particles.

Discussion

Within the cell, the degree of HBc oligomerization was never studied. In this work we investigated HBV capsid assembly in Huh7 hepatoma mammalian cells by combining FLIM-FRET, FCS and TEM. Combination of modern imaging techniques had previously been used to image the assembly of HTLV, RSV or HIV and to quantify the interaction between viral

and cellular partners [47, 48, 59-66]. These approaches provided data that revolutionized our knowledge of the dynamic and structural changes involved during viruses infectious cycle (for reviews see [67-70]) as well as in other fields of biology [71].

By using fluorescent protein tags, we show here that HBc/HBc-eGFP forms capsids in Huh7 cells similarly to wild-type capsids (Fig. 6 and Fig. S1). The FRET efficiency of HBc-eGFP found in our experiments remained similar 24, 48 and 72 hours post transfection. This suggests that the core oligomerisation happens shortly after expression and that the oligomers are not more condensed when the protein concentration increases (Fig. 3, images d, e and f). This oligomerization observed without major structural changes along the time is consistent with the homogeneous distribution of the particle size found by FCS data (Fig. 5F). The average brigthness of 26.4 times the brightness of a single eGFP corresponds to an average number of HBc per oligomer between 170 to 230 (considering the expression of dark HBc). This average number fits with the quantity of 180 or 240 of HBc units (depending on the T=4 or T=3 icosahedral symmetry) found in HBV capsid structure [25, 28].

Next, we used brightness analysis of FCS measurements that allows to discriminate monomers from oligomers to measure the assembly binding curve and to determine an apparent Kd for HBV capsid assembly of 0.7 - 0.8 µM (Fig. 5G). Interestingly, the use of brightness to measure protein-protein interaction inside living cells was already used to calculate the self-association of nuclear receptors with an apparent Kd of a few µM [72]. Similarly, the concentration of HTLV Gag and HIV Gag forming particles in living cells determined by brightness analysis was ~0.5 µM [73] with a stoichiometry for HIV ranging 750 to 2500 copies of protein per particle. This is in agreement with the larger size of HIV virus compared to HBV [74]. All these results illustrate that the brightness analysis provides details of molecular complexes in cells that would be difficult to obtain with other techniques.

In this work, a high level of HBc was imaged in the nucleus (Fig. 2) in contrast to HBc staining in replicative cells [45]. In our condition of HBc expressed alone in Huh7 mammalian cells, HBc-CTD is phosphorylated and HBV capsid free of host nucleic acid with a partial exposure of HBc-CTD on the exterior of the capsid [14-16, 19, 75-77]. In turn, the NLS comprised in the CTD is available to drive HBc nuclear import [78, 79] and, together with a nonspecific, but high affinity of HBc-CTD for double stranded DNAs [9], to favor HBc accumulation in the nucleus. Our results also show that capsids containing a mixture of unlabelled and labelled HBc form are properly organized and sized (Fig. 6a) like HBV capsids observed in cells replicating HBV (Fig. S1). HBc assembly is so independant from other viral factors or from the maturation of the capsid during the reverse transcription of the pgRNA. In addition, we found by FRET that wild type HBc efficiently oligomerize (Fig. 4 and 5A, 5E) and oligomers are homogeneously distributed within the entire cell (Fig. 3). This result shows that the assembly of HBV capsid is not restricted to a cellular sub-compartment, as described for herpes viruses in the nuclear compartment [80] or retroviruses at the plasma membrane [81]. Moreover, no significant difference in FRET efficiency or FCS measurements was observed in the nucleus as compared to the cytoplasm, despite the fact that a structural reorganization of the capsid was proposed for it to enter the nucleus [82]. In fact, in our experiments, the HBc protein was expressed alone and, as a consequence, potential structural reorganizations mediated by HBV maturation or its nuclear entry were not properly occurring [82]. Furthemore, it was proposed that the nuclear import of HBc oligomers is different from the nuclear import of viral particles competent for replication [37].

In contrast to the wild type HBc, a low FRET efficiency was observed in cell expressing HBc-NTD indicating a weak, if any, formation of HBc-NTD oligomers (Fig. 3 and 4). The low FRET was not due to a reorganization of oligomers with a larger distance between donor and acceptor, since HBc-NTD was indeed essentially observed as monomeric protein by FCS (Fig

5 E, F, G). This impairment of HBc-NTD to assemble was also confirmed by the absence of spherical, ordered complexes by TEM (Fig. 6b). This low FRET efficiency (Fig. 4) and brightness (Fig. 5F) for HBc-NTD were constant for all the post transfection timepoints analyzed, so that the lack of HBc-NTD oligomerization was not rescued by a higher concentration of protein. Indeed, no HBc-NTD oligomerization was found, even with up to 6-7 µM of HBc-NTD labelled protein (Fig. 5G). Interestingly, labelled HBc-NTD produced in millimolar concentrations in *E coli* is able to form such capsids [34, 36]. Nevertheless, in the more physiological conditions we used in this work no capsid was detected with labelled HBc-NTD, emphasizing the essential role of the CTD in HBV capsid morphogenesis.

The inefficiency of HBc-NTD to form HBc capsid when purified from a rabbit reticulocyte mammalian cells lysates had previously been reported by the group of Hu et al [32]. Our analysis using quantitative methods confirms and extends this observation. How to explain this important difference between HBc and HBc-NTD assembly in a cell context? It is possible that the absence of HBc-NTD capsid assembly in our condition results from the low concentration of expressed protein, since purified HBc-NTD was shown *in vitro* to assemble with a $K_{d\ apparent}$ of 15 µM at 0.15 M of NaCl. Alternatively, HBc-NTD assembly cannot take place in cellular conditions due to the lack of CTD. It has long been suspected that the C terminus facilitates the formation of the native shell capsid, probably via specific or nonspecific interactions with RNA [13, 44, 83]. Nevertheless, as aformentionned when HBc is expressed alone in Huh7 mammalian cells, the CTD is phosphorylated and HBV capsid frees of host nucleic acid [19, 75, 77]. Therefore, it is likely that the differences observed between HBc and HBc-NTD are due to a defect in protein-protein interactions mediated by electrostatic interactions, as recently proposed by the group of Nassal [19] and by the use of CTD phosphomimetic 7E mutant [44]. Moreover, it is known that the CTD interacts with the SRPK protein and it was proposed that, in addition to participating to CTD phosphorylation,

SRPK could act as a potent protein chaperone that facilitates HBV capsid assembly [14]. The fact that a viral protein can hijack the cellular chaperone machinery during morphogenesis has been shown for other plant or animal viruses [84].

To further confirm that the quantitative fluorescent microscopy measurements on HBc-eGFP expressed in live cells is an efficient tool to study HBc assembly, we deleted two different domains of the protein to follow its effect on the assembly of the core particle. The third helix, together with the fourth helix, belongs to the α-helical hairpin protruding at the surface of the capsid. HBc dimers are stabilized through close contacts between helix 3 of each monomer, but not with helix 4 [25, 85]. When the third helix was removed, we unexpectedly found a high FRET efficiency and the formation of large oligomers. Both FRET efficiency (Fig. 3, 4) and FCS analyses (Fig. 5C, 5F) were sensitive to the concentration of HBc-ΔαH3 proteins. FRET efficiency at 72h post transfection is similar to the FRET efficiency of the wild-type protein, except for its distribution exhibiting a large standard deviation and suggesting heterogeneous oligomers. In agreement with this heterogeneity, fluorescent particles with fast or slow diffusion coefficients were observed (Fig. 5 C). Despite these results, we never observed any capsid structure in TEM, but only the clustering of gold beads (Fig. 6c) up to 72 h post transfection (data not shown). This ability of HBc-ΔαH3 to oligomerize, although a non-canonical structure (Fig. 6c), could be explained by the presence of ^{124}VWIRTPPAYRPP^{135} domain, since its deletion in the HBcΔ124-135 constructs has a dramatic impact on HBc oligomerisation (Fig. 3-6). This sequence contains the end of the fifth helix and the proline-rich loop essential for dimer-dimer interactions [25]. Mutations of R127 to L or Q was shown to clearly affect the *in vitro* assembly of HBc-NTD expressed from *E coli* [85].

In conclusion, the knowledges gained in these studies provide novel insights to describe the spatio-temporal behavior of the HBc protein. FRET and FCS allowed to follow the assembly

of HBc, while TEM allowed the observation of HBV capsids. We found that HBV assembly occurs efficiently at a low protein concentration, regardless of its cellular localization. The loss of the C-terminus is detrimental to such assembly, and is not rescued by raising the protein concentration. These results are important for the analysis of processes involved in HBc oligomerisation such as phosphorylation [8], or the role of host proteins acting as chaperones and regulating the assembly of this viral capsid [14]. Furthermore, these studies could be used to detail the dynamics of CAMs-mediated capsid assembly inhibition and to follow the ultrastructure behavior of these complexes.

Materials and methods

Plasmid DNA

The pTURF plasmids encoding for HBc and HBc-NTD, subtype ayw, fused to eGFP (also referred below to as Fluorescent Protein, FP) was kindly provided by M Nassal [34]. FP is surrounded by flexible glycine linkers and inserted in the c/e1 epitope. This internal fusion was shown to be well tolerated with the formation of core particles [28, 35, 86, 87 , 88]. HBc-eGFP was introduced in pcDNA3.1 by PCR and this plasmid used for the construction of unlabelled HBc and HBc-mCherry. These three plasmids were then used to generate HBc-NTD-HA/Flag, HBc-ΔαH3, HBc-Δ124-135 and their fluorescent counterparts. Primers used for amplification are summarized in Supplemental Table 1. The integrity of all plasmid constructs was assessed by DNA sequencing.

Cell culture and plasmid DNA transfection

Huh7 (differentiated hepatocyte-derived carcinoma cell line) were cultured in Dulbecco's modified eagle medium supplemented with 10% fetal calf serum (DMEM + GlutaMAX, Gibco, Lifetech, France) and 1% of an antibiotic mixture

(penicillin/streptomycin: Invitrogen Corporation Pontoise, France) at 37°C in a 5% CO_2 atmosphere. Huh7 cells were transfected or co-transfected using jetPEI^{TM} (Life Technologies, Saint Aubin, France) according to the supplier's recommendations. To keep a constant amount of transfected DNA, each transfection assay was supplemented with $pcDNA_3$.

Western blot

24 h post-transfection, Huh7 cells were washed with phosphate buffered saline (PBS 1X - 140 mM NaCl, 8 mM NaH_2PO_4, 2 mM Na_2HPO_4), treated with trypsin and resuspended in ice-cold lysis buffer (1% Triton X-100, 100 mM NaF, 10 mM NaPPi, 1 mM Na3VO4 in PBS supplemented with a complete anti-protease cocktail from Roche, Meylan, France). After centrifugation, total protein concentration was assessed by Bradford analysis (Bio-Rad), and 30 µg of total protein were loaded on a 12% SDS-PAGE. Proteins were then transferred onto PDVF membrane (Amersham, Orsay, France), and blots were probed with a human anti-HBc polyclonal anti-body (dilution 1:5000) [89] or with anti-HA antibody (AB18181, dilution 1:2000) followed by horseradish peroxidase conjugated rat anti-human (southern biotch, dilution 1:20000) or rat anti-mouse (souther biotech, dilution 1:10000), revealed by chemiluminescent ECL Prime system on a Imagequant LAS500 apparatus (GE healthcare).

Confocal microscopy

8 10^4 Huh7 cells were transfected in 6-well plates containing 12 mm coverslips with 1µg a DNA containing plasmids expressing for HBc (or HBc derivatives) alone or containing a mixture of plasmid expressing for HBc (or HBc derivatives) and HBc-eGFP (or HBc-eGFP derivatives) in a ratio 0.7/0.3 to mimic conditions used for FLIM experiments. Cells expressing unlabeled proteins were washed in 1 X PBS 24h post transfection, fixed by 4% of PFA, and permeabilized with 0.2% triton/PBS. Then, cells were blocked for 30 min with

0.4% of BSA in 1 X PBS, incubated with a human polyclonal anti-HBc (diluted 1:2500, [89]) and after successive washings, with Alexa 594 goat anti human (ThermoFisher scientific). DNA was stained with DAPI (2-(4-Amidinophenyl)-6-indolecarbamidine dihydrochloride, SIGMA) (1mg/ml, 1: 10000). Cell expressing unlabelled and labelled proteins were fixed by 4% of PFA, permeabilized with 0.2% triton/PBS and washed DAPI containing 1 X PBS. Fluorescence confocal images were acquired using LEICA SP8 gSTED confocal microscope equipped with 63x (NA=1.40). Excitation light was provided with laser diode at 405 nm for DAPI, an argon laser at 488 nm for Alexa 488 and white light laser at 594nm for Alexa 594.

Cell sorting using FACS

10.10^6 Huh7 cells plated in a T75 flask and transfected with 10 µg of plasmid expressing HBc were treated with trypsin and resuspended in ice-cold complete medium (DMEM, 10% FBS). Cells were then sorted by using the BD FACS Melody and gating was done using the BD FACS Chorus™ software (BD Biosciences). Cell sorting was performed with 100 µm nozzle size and sorted directly into 1.5 ml tubes containing complete medium to minimize cellular stress. After establishing the basic gating parameters, GFP positive cells (1.10^5 to 8.10^5) of each population of interest were sorted at a speed of 6000 cells/s.

Immunogold Labeling of Cryosections - Immunoelectron Microscopy

Cells expressing HBc/HBc-eGFP for 24h were sorted and fixed for 2h with 4% paraformaldehyde in phosphate buffer (pH 7.6), washed twice with PBS (pH 7.6) and included in gelatin (12%). Infusion with sucrose (2.3 M) was performed overnight at 4°C before ultrathin cryosectioning at -120°C on a Leica Microsystems FC7 cryo-ultramicrotome. Sections (80nm thickness) were retrieved with a methylcellulose (2%) / sucrose (2.3 M) mixture (1:1) and collected onto formvar/carbon-coated nickel grids. After removal of gelatin

at 37°C, sections were incubated with PBS containing 1:200 Rabbit anti-eGFP (ABCAM, ref AB6556). After six washes of PBS (5 min each), the grids were incubated with PBS containing 1:30 gold-conjugated Goat anti-Rabbit (6 nm) (Aurion, Wageningen, the Netherlands). The grids were finally washed in PBS (six washes of 2 min each), and rinsed with distilled water. The contrasting step was performed by incubating grids in a 2% uranyl acetate/ 2% methylcellulose mixture (1:10). The sections were imaged with a JEOL JEM-1011 transmission electron microscope operating at 100 kV (JEOL 1011).

Fluorescence Lifetime Imaging Microscopy (FLIM)

Huh7 cells were transfected in 24-well plates with glass bottom (Porvair sciences, ref 324041) with a DNA mixture containing plasmids expressing HBc and HBc-eGFP (ratio 0.7/0.3) or HBc and HBc-eGFP together with HBc-mCherry (ratio 0.7/0.1/0.2). The same ratio of plasmids was used for the expression of HBc-NTD, HBc-ΔαH3 and HBc-Δ124-135. This transfection was performed on three independent plates and incubated for 24h, 48h and 72h. Prior to FLIM analysis, cells were incubated in phenol red-free Leibovitz's L-15 medium (Thermo Fisher Scientific), supplemented with 20% fetal bovine serum, 1% L-glutamine and 1% penicillin–streptomycin [90].

FLIM analyses were performed in the time domain with a time-gated custom-built setup [91] and driven by Inscoper imaging suite (www.inscoper.com). Briefly, cells were excited at 480+/-10 nm using a white light laser and emission was selected using a band pass filter of 525/50 nm for GFP donor fluorescence. Fluorescence lifetime was calculated with five sequential temporal gates of 2.2 nsec each. Mean pixel-by-pixel lifetime was calculated using the following equation: $\langle\tau\rangle=\Sigma\Delta ti \cdot Ii/\Sigma Ii$ where Δti is the delay time of the ith image acquired following a laser pulse, and Ii is the pixel-by-pixel fluorescence intensity in each image. Lifetime measurements and online calculations were performed with the Inscoper

software. Pixel-by-pixel lifetime was calculated only when fluorescence intensity was above 3000 grey levels. The FRET efficiency (E) was calculated according to:

$$E=1-\frac{\tau_{DA}}{\tau_{D}} \quad (1)$$

where τ_{DA} is the lifetime of the donor in the presence of the acceptor and τ_{D} is the lifetime of the donor in the absence of the acceptor.

Fluorescence Correlation Spectroscopy (FCS)

Huh7 cells were transfected in 24-well plates with glass bottom (Porvair sciences, ref 324041) with a DNA mixture containing plasmids expressing HBc and HBc-eGFP (ratio 0.7/0.3). As described for FLIM-FRET experiments, cells were incubated for 24h, 48h and 72h and the medium was changed for phenol red-free Leibovitz's L-15 medium (Thermo Fisher Scientific), supplemented with 20% fetal bovine serum, 1% L-glutamine and 1% penicillin–streptomycin prior to analysis [90].

FCS measurements were performed using a confocal microscope with an FCS module as previously described [92, 93]. Our setup was composed of a Leica SP8 (Leica) inverted confocal microscope with a 63X water objective with correcting ring (NA 1.2) and combined with a PicoQuant time-correlated single photon counting (TCSPC) module (PicoHarp, PicoQuant). For the eGFP fluorescence, the Argon laser line at 488 nm was used and fluorescence emission at 500-550 nm was collected after the confocal pinhole using an avalanche photodiode detector (MPD, PicoQuant). FCS measurements were carried out with the Symphotime software (PicoQuant), integratd into the LAS-AF software (Leica). For each cell, the fluctuation of the fluorescence intensity in the confocal volume was analyzed by monitoring three independent points in the cytosol. These points were acquired sequentially and in non-photobleaching conditions for 30 seconds each. Photon Counting Histograms (PCH) method was used to determine the brightness of the diffusing particles. PCH data were

fitted with the FFS Data Processor software (SSTC, Minsk, Belarus) using a two species model with N1 and N2 being the number of particles of the core monomer and oligomers having q1 and q2 brightness values, respectively. q1, the brightness of the monomeric HBc-eGFP protein was fixed during the fit by using the mean of brightness value found in the same experimental conditions for a control situation where eGFP was expressed alone in living cells after the single species model fit. q2/q1 gives directly the number of HBc-eGFP molecules present in the oligomers. N1q1 + N2q2 is directly proportional to the cellular concentration of the HBc-eGFP expressed in the cell. The ratio of the concentration of the oligomeric HBc-eGFP to the total concentration of HBc-eGFP is obtained as follows:

$$R=\frac{N2q2}{N1q1+N2q2} \qquad (2)$$

and corresponds to the % of GFP in assembled particles. To measure protein concentration, we applied the following formula using Na, the Avogadro constant, and V, the volume of the confocal spot (estimated at 0.3×10^{-15} L):

$$[\text{HBc-eGFP}]=\frac{N1q1+N2q2}{Na\times V\times q1} \qquad (3)$$

Acknowledgments

We thank Stéphane Bressanelli and Giulia Bertolin for careful reading of the manuscript. We thank M Nassal for plasmids encoding HBc-eGFP. This work was supported by the INSERM, ANRS and Tours University. We also thank the Electron Microscopy (EM) Facility (IBiSA) of Tours University (http://microscopies.med.univ-tours.fr) for technical support.

Figure Legends

Figure 1: Scheme of HBc and HBc fusion constructs and western blot analysis

A: Schematic representation of HBc and HBc derivatives. Grey filled boxes correspond to NTD helical domains and dotted box to the CTD. HA/Flag tags or fluorescent reporters

mCherry or eGFP were inserted in the positions 78 and 80. B: Western blot analysis of HBc and HBc derivatives. Huh7 were transfected with a plasmid expressing HBc or HBc derivatives and harvested 24h post transfection. Proteins were heat denatured and loaded on a SDS-PAGE. HBc and HBc derivatives were revealed using anti-HBc antibody excepted for HBc-NTD-HA/Flag that was revealed with an anti-HA antibody. * corresponds to a partial hydrolysis of HBc-mCherry and HBc-mCherry derivatives.

Figure 2: Cellular localisation of HBc, HBc derivatives and their fluorescent counterparts.

Upper row: Huh7 were transfected with 1µg of plasmid expressing HBc or HBc derivatives: (a) HBc, (b) HBc-NTD, (c) HBc-ΔαH3 and (d) HBc-Δ124–135. Cells were fixed and immunostained with a human anti-HBc antibody detected with Alexa ~~fluor~~ 585 goat anti-human. The last washing was carried out with DAPI. Lower row: Huh7 were transfected with 1µg of plasmid expressing HBc or HBc derivatives together with their eGFP counterpart (ratio 0.7/0.3): (e) HBc and HBc-eGFP, (f) HBc-NTD and HBc-eGFP-NTD, (g) HBc-ΔαH3 and HBc-eGFP-ΔαH3, (h) HBc-Δ124–135 and HBc-eGFP-Δ124–135. Cells were fixed and stained with DAPI. Each image corresponds to the superimposition of the blue channel and the green channel. These images show the major observed phenotype from 5 to 10 cells of three independent experiments. Scale bar in white represents 10 µm.

Figure 3: Imaging the oligomerisation of HBc and HBc derivatives

Representative lifetime images showing the distribution of HBc-eGFP (and HBc-eGFP derivatives) proteins expressed in Huh7 cells. Cells were transfected by a plasmid expressing eGFP (a) or the chimeric eGFP-mCherry protein (b) or a mixture of HBc/HBc-eGFP (ratio 0.7/0.3) (c) together with HBc-mCherry (ratio 0.7/0.1/0.2) (d, e, f) or a mixture of HBc-

NTD/HBc-eGFP-NTD (ratio 0.7/0.3) (g) together with HBc-NTD-mCherry (ratio 0.7/0.1/0.2) (h, i, j) or a mixture of HBc-ΔαH3/HBc-ΔαH3-eGFP (ratio 0.7/0.3) (k) together with HBc-ΔαH3-mCherry (ratio 0.7/0.1/0.2) (l, m, n) or a mixture of HBc-Δ124-135/HBc-Δ124-135-eGFP (ratio 0.7/0.3) (o) together with HBc-Δ124-135-mCherry (ratio 0.7/0.1/0.2) (p, q, r). Three 24-well plates were prepared with 810^5 cells/well, incubated 37°C for 24, 48 or 72 h. Then, DMEM medium was substituted for phenol red-free Leibovitz's L-15 medium supplemented with 20% fetal bovine serum and observed in thermostatic chamber. The fluorescence lifetime τ of HBc-eGFP (or HBc-eGFP derivatives) was measured in the absence of the acceptor protein (images c, g, k and o) or in the presence of their mCherry counter parts and converted into color using a color scale ranging from orange (1 ns = short fluorescence lifetime) to red (2.6 ns = long fluorescence lifetime). A scale bar in white is reported image a and represents 10 μm.

Figure 4: Histograms of FRET efficiency as function of time post transfection.

Box and whiskers plots of the FRET efficiency (E) was determined at 24, 48 and 72h post transfection. E was calculated using the equation (1) where τ_{DA} is the lifetime of the donor in the presence of the acceptor and τ_{D} is the lifetime of the donor in the absence of the acceptor. Of note, τ_D used in the equation was determined for each HBc derivatives and at time of FLIM analysis (24h, 48h and 72h). Student tests were performed to compare the FRET efficiencies for at least 150 cells in three independent (ns: not specific; *: $p<0.05$; ***: $p<10^{-3}$).

Figure 5: Analysis of HBc or HBc derivatives particle formation through fluorescence fluctuation spectroscopy.

A-B-C-D: Single representative measurements of fluorescence fluctuation. Each panel comprises the time trace of the photon counts over the 30 seconds of the measurement (top), the autocorrelation curve (left) and the photon counting histogram (right) obtained on cells expressing A: HBc-HBc-eGFP (ratio 7/3); B: HBc-NTD-HBc-NTD-eGFP(7/3); C: HBc-ΔαH3-HBc-ΔαH3-eGFP (7/3); D: HBcΔ124-153-HBcΔ124-153-eGFP(7/3). E: Proportion of measurements where the formation of oligomeric particles was observed. F: Box-plot showing the distribution of the measurements of the number of eGFPs in the observed particles (q2/q1, see Material & Methods for details about the calculations). Top and bottom line: 1st and 3rd quartiles respectively. Middle line: median value. Whiskers: Minimum and maximum values. G: Distribution of the proportion of eGFP found in assembled particles over the concentration of eGFP in the observed confocal volume. See Materials & Methods for calculation details.

Figure 6: Immunogold labeling of HBc and HBc derivatives by cryo-electron microscopy (Tokuyasu method).

Huh7 were transiently transfected by a mixture of DNA plasmid expressing HBc (a) or HBc-NTD (b) or HBc-ΔαH3 (c) or HBc-Δ124-135 (d) together with their eGFP counterpart in a ratio 0.7/0.3. Cells were sorted by monitoring eGFP and fixed prior to gelatin inclusion. Ultrathin sections were cut (70 nm) and incubated first with rabbit anti-eGFP antibody and then with 10 nm size gold-conjugated anti-rabbit antibody. Scale is reported at the bottom left. Insets present various clusters of gold-conjugated goat anti-Rabbit. HBV capsids are highlighted by yellow arrows.

Figure S1: Immunogold labelling of HBc by cryo-electron microscopy (Tokuyasu method).

HBV capsids produced in Huh7 cells after transfection with a mixture of plasmids (ratio 0.7/0.3) expressing HBc and HBc-eGFP (Fig. 6) were compared with HBV capsid produced in HepAD38 (a) and in Huh7 cells after transfection of a plasmid expressing 1.1-fold HBV genome (b).

a: HBV particles observed in HepAD38 cell. HepAD38 cells are an inducible human hepatoblastoma cell line harboring an integrated tetracycline-responsive 1.2-fold HBV genome (serotype ayw, genotype D) [94]. HepaD38 cells were grown in DMEM supplemented with 10% fetal calf serum and 1% of an antibiotic mixture (penicillin/streptomycin) at 37°C in a 5% CO_2 atmosphere. b: Huh7 (differentiated hepatocyte-derived carcinoma cell line) were cultured in DMEM supplemented with 10% fetal calf serum and 1% of an antibiotic mixture (penicillin/streptomycin) at 37°C in a 5% CO_2 atmosphere. 10.10^6 Huh7 cells plated in a T75 flask and transfected with 9 µg of plasmid expressing 1.1-fold HBV genome (serotype ayw, genotype D) and 1µg of GFP plasmid, were treated with trypsin and resuspended in ice-cold complete medium (DMEM, 10% FBS). Cells eGFP positive were then sorted by FACS. Both cell lines were prepared for immunolabeling and imaged TEM as described in the materials and methods section. The rabbit anti-eGFP was substitutied for a human anti-HBc (dilution: 1:200, [89]) and the gold-conjugated Goat anti-Rabbit (6 nm) for a gold-conjugated Goat anti-human (dilution: 1:30; 6 nm). HBV capsids are highlighted by yellow arrows. Scale is reported at the bottom left.

Table 1: HBc and HBc-NTD assembly from various organism.

	Escherichia Coli	rabbit reticulocyte lysate (RRL)	Xenopus oocytes	HepG2.117, HuH7,	Insect cells
HBc	**+++** [11, 19, 95]	**+++** [32]	**+++** [96, 97]	**+++** [19, 98, 99]	**+++** [100]
HBc-NTD	**+++** [3, 13, 25, 29]	**-** [32]	nd	nd	nd

+++ means assembly efficiency; - means assembly deficiency

References

1. Neuveut C, Wei Y & Buendia MA. (2010). Mechanisms of HBV-related hepatocarcinogenesis. Journal of hepatology. 52, 594-604.
2. Prange R. (2012). Host factors involved in hepatitis B virus maturation, assembly, and egress. Medical microbiology and immunology. 201, 449-61.
3. Venkatakrishnan B & Zlotnick A. (2016). The Structural Biology of Hepatitis B Virus: Form and Function. Annu Rev Virol. 3, 429-51.
4. Nassal M. (2015). HBV cccDNA: viral persistence reservoir and key obstacle for a cure of chronic hepatitis B. Gut. 64, 1972-84.
5. Dane DS, Cameron CH & Briggs M. (1970). Virus-like particles in serum of patients with Australia-antigen-associated hepatitis. Lancet (London, England). 1, 695-8.
6. Blumberg BS. (1977). Australia antigen and the biology of hepatitis B. Science (New York, NY). 197, 17-25.
7. Bruss V. (2007). Hepatitis B virus morphogenesis. World journal of gastroenterology. 13, 65-73.
8. Hu J & Liu K. (2017). Complete and Incomplete Hepatitis B Virus Particles: Formation, Function, and Application. Viruses. 9.
9. Hatton T, Zhou S & Standring DN. (1992). RNA- and DNA-binding activities in hepatitis B virus capsid protein: a model for their roles in viral replication. Journal of virology. 66, 5232-41.
10. Nassal M. (1992). The arginine-rich domain of the hepatitis B virus core protein is required for pregenome encapsidation and productive viral positive-strand DNA synthesis but not for virus assembly. Journal of virology. 66, 4107-16.
11. Porterfield JZ, Dhason MS, Loeb DD, Nassal M, Stray SJ & Zlotnick A. (2010). Full-length hepatitis B virus core protein packages viral and heterologous RNA with similarly high levels of cooperativity. Journal of virology. 84, 7174-84.
12. Lewellyn EB & Loeb DD. (2011). The arginine clusters of the carboxy-terminal domain of the core protein of hepatitis B virus make pleiotropic contributions to genome replication. Journal of virology. 85, 1298-309.
13. Patel N, White SJ, Thompson RF, Bingham R, Weiss EU, Maskell DP, et al. (2017). HBV RNA pre-genome encodes specific motifs that mediate interactions with the viral core protein that promote nucleocapsid assembly. Nat Microbiol. 2, 17098.
14. Chen C, Wang JC & Zlotnick A. (2011). A kinase chaperones hepatitis B virus capsid assembly and captures capsid dynamics in vitro. PLoS pathogens. 7, e1002388.
15. Wang JC, Dhason MS & Zlotnick A. (2012). Structural organization of pregenomic RNA and the carboxy-terminal domain of the capsid protein of hepatitis B virus. PLoS pathogens. 8, e1002919.
16. Rabe B, Vlachou A, Pante N, Helenius A & Kann M. (2003). Nuclear import of hepatitis B virus capsids and release of the viral genome. Proceedings of the National Academy of Sciences of the United States of America. 100, 9849-54.
17. Gallina A, Bonelli F, Zentilin L, Rindi G, Muttini M & Milanesi G. (1989). A recombinant hepatitis B core antigen polypeptide with the protamine-like domain deleted self-assembles into capsid particles but fails to bind nucleic acids. Journal of virology. 63, 4645-52.
18. Yu X, Jin L, Jih J, Shih C & Zhou ZH. (2013). 3.5A cryoEM structure of hepatitis B virus core assembled from full-length core protein. PloS one. 8, e69729.

19. Heger-Stevic J, Zimmermann P, Lecoq L, Bottcher B & Nassal M. (2018). Hepatitis B virus core protein phosphorylation: Identification of the SRPK1 target sites and impact of their occupancy on RNA binding and capsid structure. PLoS pathogens. 14, e1007488.
20. Watts NR, Conway JF, Cheng N, Stahl SJ, Belnap DM, Steven AC, et al. (2002). The morphogenic linker peptide of HBV capsid protein forms a mobile array on the interior surface. Embo j. 21, 876-84.
21. Liu K, Luckenbaugh L, Ning X, Xi J & Hu J. (2018). Multiple roles of core protein linker in hepatitis B virus replication. PLoS pathogens. 14, e1007085.
22. Chu TH, Liou AT, Su PY, Wu HN & Shih C. (2014). Nucleic acid chaperone activity associated with the arginine-rich domain of human hepatitis B virus core protein. Journal of virology. 88, 2530-43.
23. Gallucci L & Kann M. (2017). Nuclear Import of Hepatitis B Virus Capsids and Genome. Viruses. 9.
24. Martinez MG, Testoni B & Zoulim F. (2019). Biological basis for functional cure of chronic hepatitis B. Journal Of Viral Hepatitis. 26, 786-94.
25. Wynne SA, Crowther RA & Leslie AG. (1999). The crystal structure of the human hepatitis B virus capsid. Mol Cell. 3, 771-80.
26. Bottcher B, Wynne SA & Crowther RA. (1997). Determination of the fold of the core protein of hepatitis B virus by electron cryomicroscopy. Nature. 386, 88-91.
27. Conway JF, Cheng N, Zlotnick A, Wingfield PT, Stahl SJ & Steven AC. (1997). Visualization of a 4-helix bundle in the hepatitis B virus capsid by cryo-electron microscopy. Nature. 386, 91-4.
28. Crowther RA, Kiselev NA, Bottcher B, Berriman JA, Borisova GP, Ose V, et al. (1994). Three-dimensional structure of hepatitis B virus core particles determined by electron cryomicroscopy. Cell. 77, 943-50.
29. Zlotnick A, Cheng N, Conway JF, Booy FP, Steven AC, Stahl SJ, et al. (1996). Dimorphism of hepatitis B virus capsids is strongly influenced by the C-terminus of the capsid protein. Biochemistry. 35, 7412-21.
30. Bourne CR, Finn MG & Zlotnick A. (2006). Global structural changes in hepatitis B virus capsids induced by the assembly effector HAP1. Journal of virology. 80, 11055-61.
31. Selzer L, Katen SP & Zlotnick A. (2014). The hepatitis B virus core protein intradimer interface modulates capsid assembly and stability. Biochemistry. 53, 5496-504.
32. Ludgate L, Liu K, Luckenbaugh L, Streck N, Eng S, Voitenleitner C, et al. (2016). Cell-Free Hepatitis B Virus Capsid Assembly Dependent on the Core Protein C-Terminal Domain and Regulated by Phosphorylation. Journal of virology. 90, 5830-44.
33. Sun D & Nassal M. (2006). Stable HepG2- and Huh7-based human hepatoma cell lines for efficient regulated expression of infectious hepatitis B virus. Journal of hepatology. 45, 636-45.
34. Kratz PA, Bottcher B & Nassal M. (1999). Native display of complete foreign protein domains on the surface of hepatitis B virus capsids. Proceedings of the National Academy of Sciences of the United States of America. 96, 1915-20.
35. Vogel M, Diez M, Eisfeld J & Nassal M. (2005). In vitro assembly of mosaic hepatitis B virus capsid-like particles (CLPs): rescue into CLPs of assembly-deficient core protein fusions and FRET-suited CLPs. FEBS letters. 579, 5211-6.
36. Yoo L, Park JS, Kwon KC, Kim SE, Jin X, Kim H, et al. (2012). Fluorescent viral nanoparticles with stable in vitro and in vivo activity. Biomaterials. 33, 6194-200.
37. Weigand K, Knaust A & Schaller H. (2010). Assembly and export determine the intracellular distribution of hepatitis B virus core protein subunits. J Gen Virol. 91, 59-67.
38. Chen JY, Gan CY, Cai XF, Zhang WL, Long QX, Wei XF, et al. (2018). Fluorescent protein tagged hepatitis B virus capsid protein with long glycine-serine linker that supports nucleocapsid formation. Journal of virological methods. 255, 52-9.
39. Schodel F, Wirtz R, Peterson D, Hughes J, Warren R, Sadoff J, et al. (1994). Immunity to malaria elicited by hybrid hepatitis B virus core particles carrying circumsporozoite protein epitopes. The Journal of experimental medicine. 180, 1037-46.
40. Boulter NR, Glass EJ, Knight PA, Bell-Sakyi L, Brown CG & Hall R. (1995). Theileria annulata sporozoite antigen fused to hepatitis B core antigen used in a vaccination trial. Vaccine. 13, 1152-60.

41. Shaner NC, Steinbach PA & Tsien RY. (2005). A guide to choosing fluorescent proteins. Nat Methods. 2, 905-9.
42. Vogel M, Vorreiter J & Nassal M. (2005). Quaternary structure is critical for protein display on capsid-like particles (CLPs): efficient generation of hepatitis B virus CLPs presenting monomeric but not dimeric and tetrameric fluorescent proteins. Proteins. 58, 478-88.
43. Ning X, Luckenbaugh L, Liu K, Bruss V, Sureau C & Hu J. (2018). Common and Distinct Capsid and Surface Protein Requirements for Secretion of Complete and Genome-Free Hepatitis B Virions. Journal of virology. 92.
44. Ludgate L, Liu K, Luckenbaugh L, Streck N, Eng S, Voitenleitner C, et al. (2016). Cell-Free Hepatitis B Virus Capsid Assembly Dependent on the Core Protein C-Terminal Domain and Regulated by Phosphorylation. Journal of virology. 90, 5830-44.
45. Deroubaix A, Osseman Q, Cassany A, Begu D, Ragues J, Kassab S, et al. (2015). Expression of viral polymerase and phosphorylation of core protein determine core and capsid localization of the human hepatitis B virus. J Gen Virol. 96, 183-95.
46. Rat V, Seigneuret F, Burlaud-Gaillard J, Lemoine R, Hourioux C, Zoulim F, et al. (2019). BAY 41-4109-mediated aggregation of assembled and misassembled HBV capsids in cells revealed by electron microscopy. Antiviral research. 169, 104557.
47. El Meshri SE, Dujardin D, Godet J, Richert L, Boudier C, Darlix JL, et al. (2015). Role of the Nucleocapsid Domain in HIV-1 Gag Oligomerization and Trafficking to the Plasma Membrane: A Fluorescence Lifetime Imaging Microscopy Investigation. J Mol Biol. 427, 1480-94.
48. Maldonado JO, Angert I, Cao S, Berk S, Zhang W, Mueller JD, et al. (2017). Perturbation of Human T-Cell Leukemia Virus Type 1 Particle Morphology by Differential Gag Co-Packaging. Viruses. 9.
49. Tramier M, Zahid M, Mevel JC, Masse MJ & Coppey-Moisan M. (2006). Sensitivity of CFP/YFP and GFP/mCherry pairs to donor photobleaching on FRET determination by fluorescence lifetime imaging microscopy in living cells. Microscopy research and technique. 69, 933-9.
50. Padilla-Parra S & Tramier M. (2012). FRET microscopy in the living cell: different approaches, strengths and weaknesses. BioEssays : news and reviews in molecular, cellular and developmental biology. 34, 369-76.
51. Richert L, Didier P, de Rocquigny H & Mély Y. (2015). Monitoring HIV-1 Protein Oligomerization by FLIM FRET Microscopy Advanced Time-Correlated Single Photon Counting Applications

Springer Series in Chemical Physics. 111, 277-307.
52. Pepperkok R, Squire A, Geley S & Bastiaens PI. (1999). Simultaneous detection of multiple green fluorescent proteins in live cells by fluorescence lifetime imaging microscopy. Curr Biol. 9, 269-72.
53. Merzlyak EM, Goedhart J, Shcherbo D, Bulina ME, Shcheglov AS, Fradkov AF, et al. (2007). Bright monomeric red fluorescent protein with an extended fluorescence lifetime. Nat Methods. 4, 555-7.
54. Albertazzi L, Arosio D, Marchetti L, Ricci F & Beltram F. (2009). Quantitative FRET analysis with the EGFP-mCherry fluorescent protein pair. Photochemistry and photobiology. 85, 287-97.
55. Kumar S, Alibhai D, Margineanu A, Laine R, Kennedy G, McGinty J, et al. (2011). FLIM FRET technology for drug discovery: automated multiwell-plate high-content analysis, multiplexed readouts and application in situ. Chemphyschem : a European journal of chemical physics and physical chemistry. 12, 609-26.
56. Teitler M & Herrick-Davis K. (2014). Determining the oligomer number of native GPCR using florescence correlation spectroscopy and drug-induced inactivation-reactivation. Current pharmaceutical biotechnology. 15, 927-37.
57. Walter A, Chapuis C, Huet S & Ellenberg J. (2013). Crowded chromatin is not sufficient for heterochromatin formation and not required for its maintenance. Journal of structural biology. 184, 445-53.
58. Macdonald P, Johnson J, Smith E, Chen Y & Mueller JD. (2013). Brightness analysis. Methods Enzymol. 518, 71-98.

59. Fogarty KH, Berk S, Grigsby IF, Chen Y, Mansky LM & Mueller JD. (2014). Interrelationship between cytoplasmic retroviral Gag concentration and Gag-membrane association. J Mol Biol. 426, 1611-24.
60. Larson DR, Ma YM, Vogt VM & Webb WW. (2003). Direct measurement of Gag-Gag interaction during retrovirus assembly with FRET and fluorescence correlation spectroscopy. J Cell Biol. 162, 1233-44.
61. Hogue IB, Hoppe A & Ono A. (2009). Quantitative fluorescence resonance energy transfer microscopy analysis of the human immunodeficiency virus type 1 Gag-Gag interaction: relative contributions of the CA and NC domains and membrane binding. J Virol. 83, 7322-36.
62. Hendrix J, Baumgartel V, Schrimpf W, Ivanchenko S, Digman MA, Gratton E, et al. (2015). Live-cell observation of cytosolic HIV-1 assembly onset reveals RNA-interacting Gag oligomers. J Cell Biol. 210, 629-46.
63. Ferrer M, Henriet S, Chamontin C, Laine S & Mougel M. (2016). From Cells to Virus Particles: Quantitative Methods to Monitor RNA Packaging. Viruses. 8.
64. Ivanchenko S, Godinez WJ, Lampe M, Krausslich HG, Eils R, Rohr K, et al. (2009). Dynamics of HIV-1 assembly and release. PLoS pathogens. 5, e1000652.
65. Prescher J, Baumgartel V, Ivanchenko S, Torrano AA, Brauchle C, Muller B, et al. (2015). Super-resolution imaging of ESCRT-proteins at HIV-1 assembly sites. PLoS pathogens. 11, e1004677.
66. Favard C, Chojnacki J, Merida P, Yandrapalli N, Mak J, Eggeling C, et al. (2019). HIV-1 Gag specifically restricts PI(4,5)P2 and cholesterol mobility in living cells creating a nanodomain platform for virus assembly. Science advances. 5, eaaw8651.
67. Chojnacki J & Muller B. (2013). Investigation of HIV-1 assembly and release using modern fluorescence imaging techniques. Traffic (Copenhagen, Denmark). 14, 15-24.
68. Inamdar K, Floderer C, Favard C & Muriaux D. (2019). Monitoring HIV-1 Assembly in Living Cells: Insights from Dynamic and Single Molecule Microscopy. Viruses. 11.
69. Jouvenet N, Simon SM & Bieniasz PD. (2011). Visualizing HIV-1 assembly. J Mol Biol. 410, 501-11.
70. Sharma KK, Marzinek JK, Tantirimudalige SN, Bond PJ & Wohland T. (2019). Single-molecule studies of flavivirus envelope dynamics: Experiment and computation. Progress in biophysics and molecular biology. 143, 38-51.
71. Veerapathiran S & Wohland T. (2018). Fluorescence techniques in developmental biology. Journal of biosciences. 43, 541-53.
72. Chen Y, Wei LN & Muller JD. (2003). Probing protein oligomerization in living cells with fluorescence fluctuation spectroscopy. Proceedings of the National Academy of Sciences of the United States of America. 100, 15492-7.
73. Fogarty KH, Chen Y, Grigsby IF, Macdonald PJ, Smith EM, Johnson JL, et al. (2011). Characterization of cytoplasmic Gag-gag interactions by dual-color z-scan fluorescence fluctuation spectroscopy. Biophysical journal. 100, 1587-95.
74. Chen Y, Wu B, Musier-Forsyth K, Mansky LM & Mueller JD. (2009). Fluorescence fluctuation spectroscopy on viral-like particles reveals variable gag stoichiometry. Biophysical journal. 96, 1961-9.
75. Zhao Q, Hu Z, Cheng J, Wu S, Luo Y, Chang J, et al. (2018). Hepatitis B Virus Core Protein Dephosphorylation Occurs during Pregenomic RNA Encapsidation. Journal of virology. 92.
76. Jung J, Hwang SG, Chwae YJ, Park S, Shin HJ & Kim K. (2014). Phosphoacceptors threonine 162 and serines 170 and 178 within the carboxyl-terminal RRRS/T motif of the hepatitis B virus core protein make multiple contributions to hepatitis B virus replication. Journal of virology. 88, 8754-67.
77. Su P-Y, Yang C-J, Chu T-H, Chang C-H, Chiang C, Tang F-M, et al. HBV maintains electrostatic homeostasis by modulating negative charges from phosphoserine and encapsidated nucleic acids. Scientific reports2016. p. 38959.
78. Yeh CT, Liaw YF & Ou JH. (1990). The arginine-rich domain of hepatitis B virus precore and core proteins contains a signal for nuclear transport. Journal of virology. 64, 6141-7.

79. Kann M, Sodeik B, Vlachou A, Gerlich WH & Helenius A. (1999). Phosphorylation-dependent binding of hepatitis B virus core particles to the nuclear pore complex. The Journal of cell biology. 145, 45-55.
80. Mettenleiter TC. (2002). Herpesvirus assembly and egress. Journal of virology. 76, 1537-47.
81. Sundquist WI & Krausslich HG. (2012). HIV-1 assembly, budding, and maturation. Cold Spring Harbor perspectives in medicine. 2, a006924.
82. Rabe B, Delaleau M, Bischof A, Foss M, Sominskaya I, Pumpens P, et al. (2009). Nuclear entry of hepatitis B virus capsids involves disintegration to protein dimers followed by nuclear reassociation to capsids. PLoS pathogens. 5, e1000563.
83. Zlotnick A, Porterfield JZ & Wang JC. (2013). To build a virus on a nucleic acid substrate. Biophysical journal. 104, 1595-604.
84. Dokland T. (1999). Scaffolding proteins and their role in viral assembly. Cellular and molecular life sciences : CMLS. 56, 580-603.
85. Konig S, Beterams G & Nassal M. (1998). Mapping of homologous interaction sites in the hepatitis B virus core protein. Journal of virology. 72, 4997-5005.
86. Nassal M, Skamel C, Kratz PA, Wallich R, Stehle T & Simon MM. (2005). A fusion product of the complete Borrelia burgdorferi outer surface protein A (OspA) and the hepatitis B virus capsid protein is highly immunogenic and induces protective immunity similar to that seen with an effective lipidated OspA vaccine formula. Eur J Immunol. 35, 655-65.
87. Geldmacher A, Skrastina D, Petrovskis I, Borisova G, Berriman JA, Roseman AM, et al. (2004). An amino-terminal segment of hantavirus nucleocapsid protein presented on hepatitis B virus core particles induces a strong and highly cross-reactive antibody response in mice. Virology. 323, 108-19.
88. Park JS, Cho MK, Lee EJ, Ahn KY, Lee KE, Jung JH, et al. (2009). A highly sensitive and selective diagnostic assay based on virus nanoparticles. Nat Nanotechnol. 4, 259-64.
89. Roingeard P, Romet-Lemonne JL, Leturcq D, Goudeau A & Essex M. (1990). Hepatitis B virus core antigen (HBc Ag) accumulation in an HBV nonproducer clone of HepG2-transfected cells is associated with cytopathic effect. Virology. 179, 113-20.
90. Bertolin G, Sizaire F, Herbomel G, Reboutier D, Prigent C & Tramier M. (2016). A FRET biosensor reveals spatiotemporal activation and functions of aurora kinase A in living cells. Nature communications. 7, 12674.
91. Leray A, Padilla-Parra S, Roul J, Heliot L & Tramier M. (2013). Spatio-Temporal Quantification of FRET in living cells by fast time-domain FLIM: a comparative study of non-fitting methods [corrected]. PloS one. 8, e69335.
92. Ziegler CS, Bouchab L, Tramier M, Durand D, Fieschi F, Dupre-Crochet S, et al. (2019). Quantitative live-cell imaging and 3D modeling reveal critical functional features in the cytosolic complex of phagocyte NADPH oxidase. The Journal of biological chemistry. 294, 3824-36.
93. Bertolin G, Sizaire F, Demeautis C, Chapuis C, Merola F, Erard M, et al. (2019). Optimized FRET Pairs and Quantification Approaches To Detect the Activation of Aurora Kinase A at Mitosis. ACS sensors. 4, 2018-27.
94. Ladner SK, Otto MJ, Barker CS, Zaifert K, Wang GH, Guo JT, et al. (1997). Inducible expression of human hepatitis B virus (HBV) in stably transfected hepatoblastoma cells: a novel system for screening potential inhibitors of HBV replication. Antimicrobial agents and chemotherapy. 41, 1715-20.
95. Wingfield PT, Stahl SJ, Williams RW & Steven AC. (1995). Hepatitis core antigen produced in Escherichia coli: subunit composition, conformational analysis, and in vitro capsid assembly. Biochemistry. 34, 4919-32.
96. Yang SQ, Walter M & Standring DN. (1992). Hepatitis B virus p25 precore protein accumulates in Xenopus oocytes as an untranslocated phosphoprotein with an uncleaved signal peptide. Journal of virology. 66, 37-45.
97. Seifer M, Zhou S & Standring DN. (1993). A micromolar pool of antigenically distinct precursors is required to initiate cooperative assembly of hepatitis B virus capsids in Xenopus oocytes. Journal of virology. 67, 249-57.

98. Ponsel D & Bruss V. (2003). Mapping of amino acid side chains on the surface of hepatitis B virus capsids required for envelopment and virion formation. Journal of virology. 77, 416-22.
99. Koschel M, Oed D, Gerelsaikhan T, Thomssen R & Bruss V. (2000). Hepatitis B virus core gene mutations which block nucleocapsid envelopment. Journal of virology. 74, 1-7.
100. Lanford RE & Notvall L. (1990). Expression of hepatitis B virus core and precore antigens in insect cells and characterization of a core-associated kinase activity. Virology. 176, 222-33.

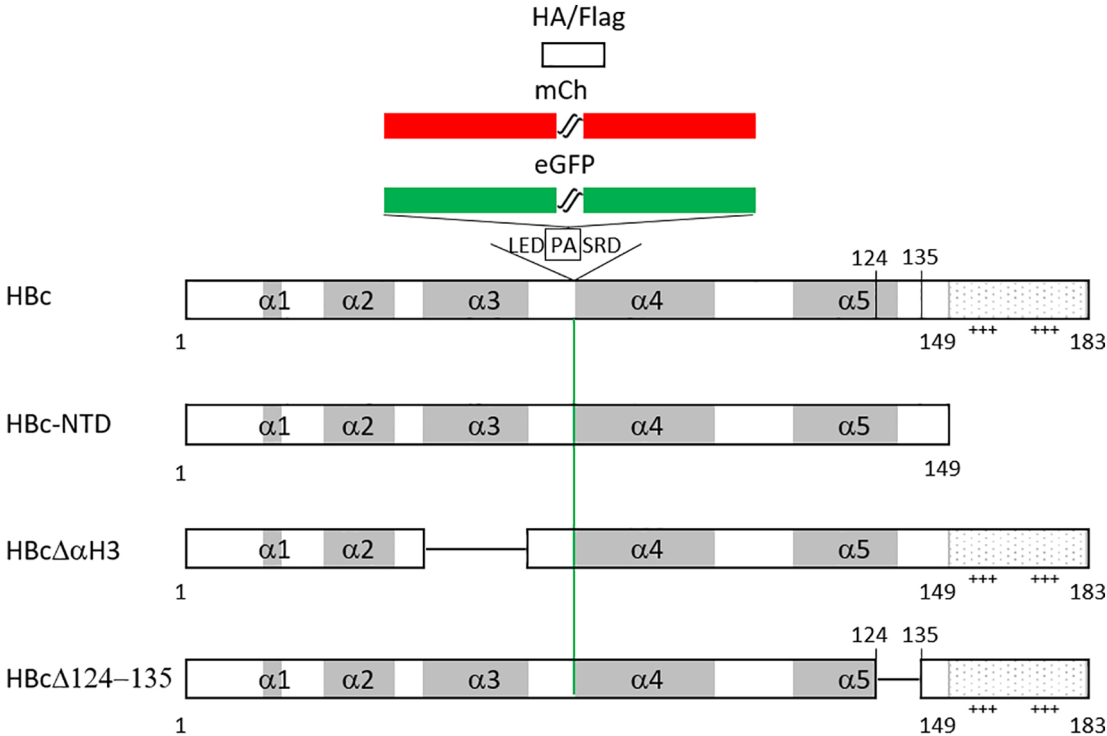
HA/Flag
mCh
eGFP
LED PA SRD
HBc
α1 α2 α3 α4 α5
124 135
1 149 +++ +++ 183
HBc-NTD
1 149
HBcΔαH3
1 149 +++ +++ 183
HBcΔ124–135
1 149 +++ +++ 183

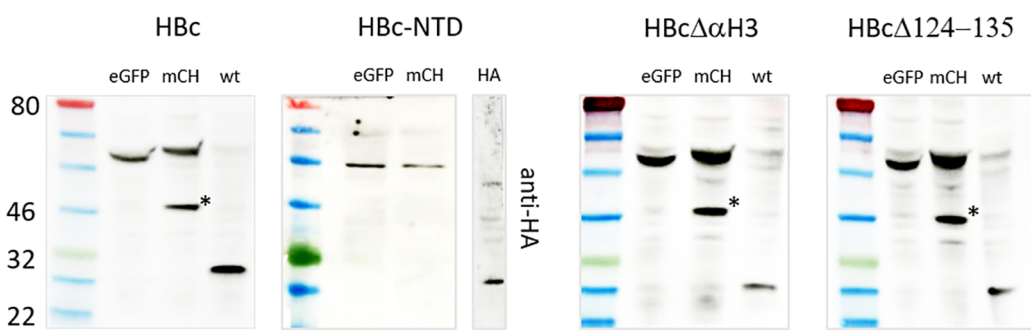
HBc
eGFP mCH wt
HBc-NTD
eGFP mCH HA
HBcΔαH3
eGFP mCH wt
HBcΔ124–135
eGFP mCH wt
80
46
32
22
*
anti-HA

Figure 1

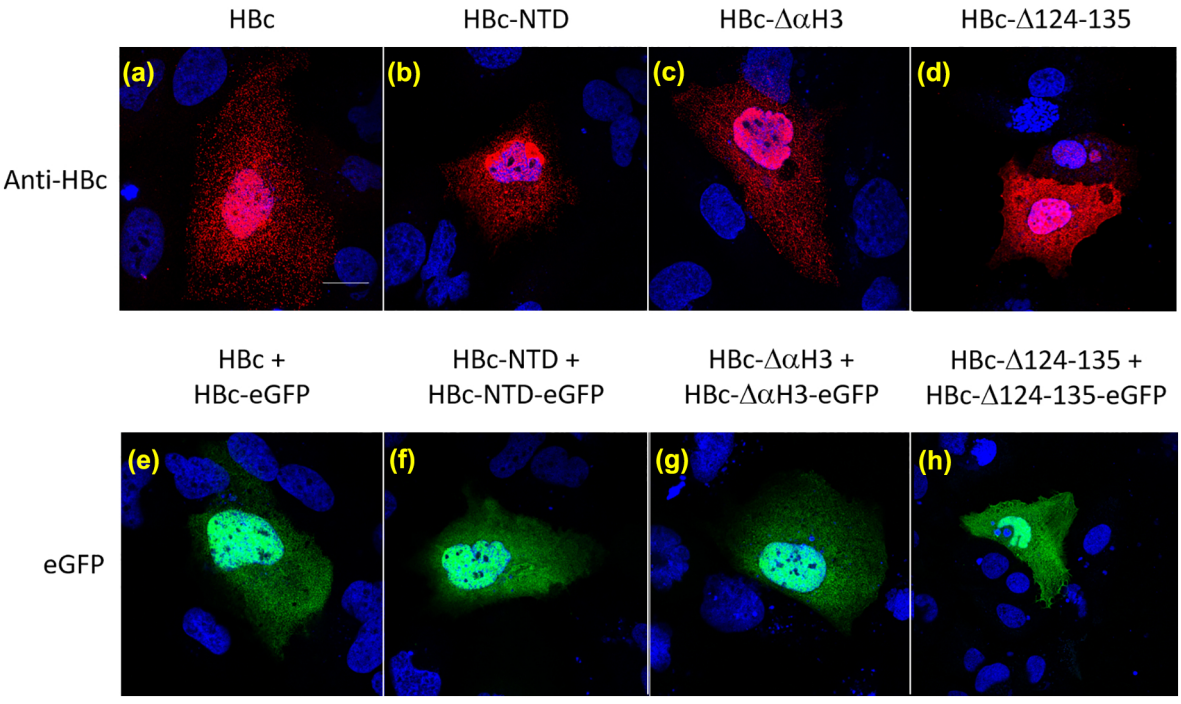
HBc
HBc-NTD
HBc-ΔαH3
HBc-Δ124-135
Anti-HBc
(a)
(b)
(c)
(d)
HBc +
HBc-eGFP
HBc-NTD +
HBc-NTD-eGFP
HBc-ΔαH3 +
HBc-ΔαH3-eGFP
HBc-Δ124-135 +
HBc-Δ124-135-eGFP
eGFP
(e)
(f)
(g)
(h)

Figure 2

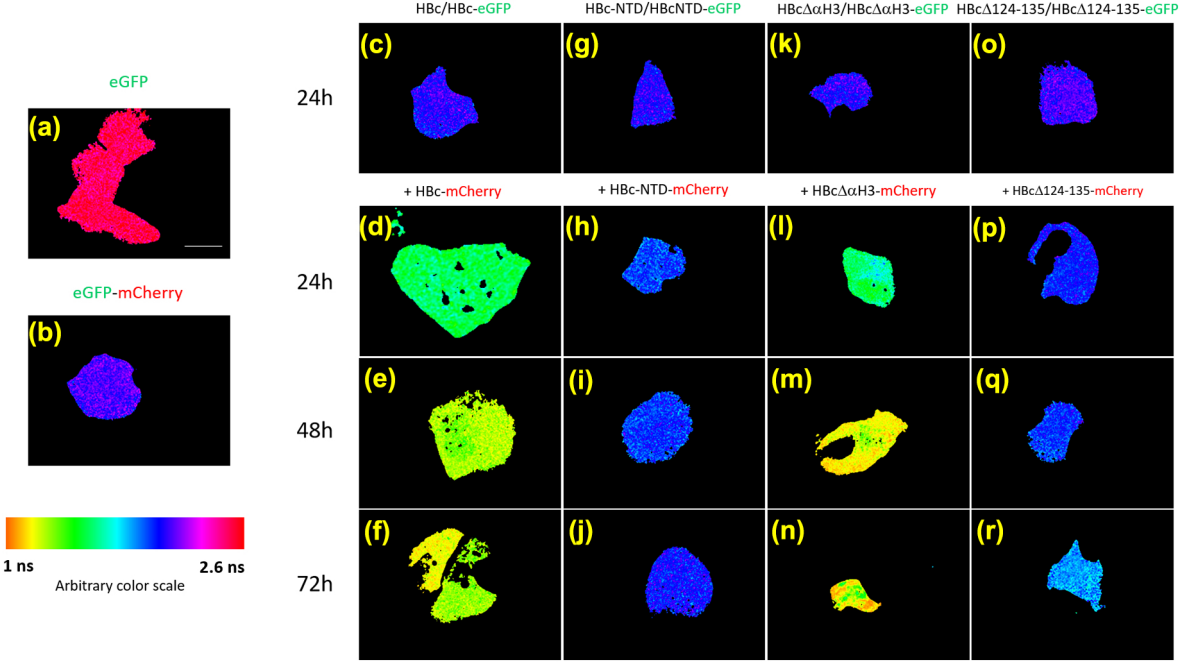
eGFP
(a)
eGFP-mCherry
(b)
1 ns
2.6 ns
Arbitrary color scale
HBc/HBc-eGFP
HBc-NTD/HBcNTD-eGFP
HBcΔαH3/HBcΔαH3-eGFP
HBcΔ124-135/HBcΔ124-135-eGFP
24h
(c)
(g)
(k)
(o)
+ HBc-mCherry
+ HBc-NTD-mCherry
+ HBcΔαH3-mCherry
+ HBcΔ124-135-mCherry
24h
(d)
(h)
(l)
(p)
48h
(e)
(i)
(m)
(q)
72h
(f)
(j)
(n)
(r)

Figure 3

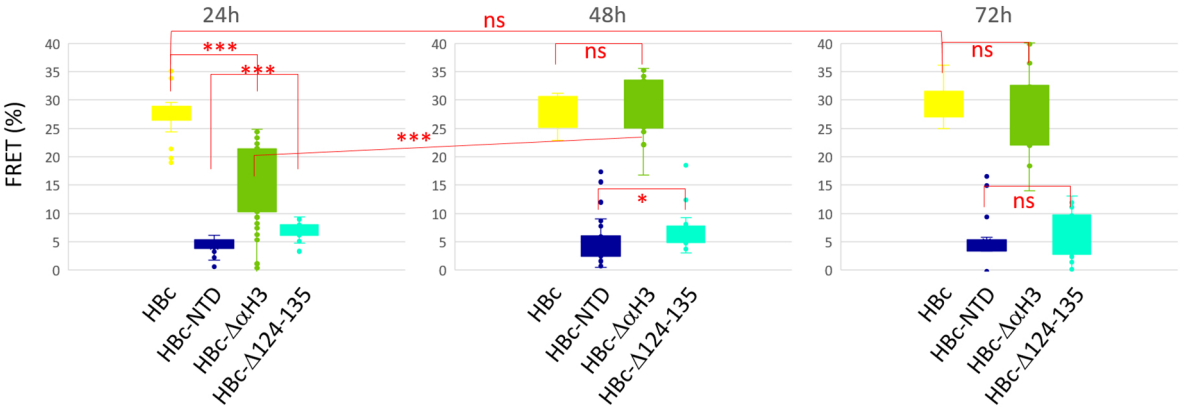

Figure 4

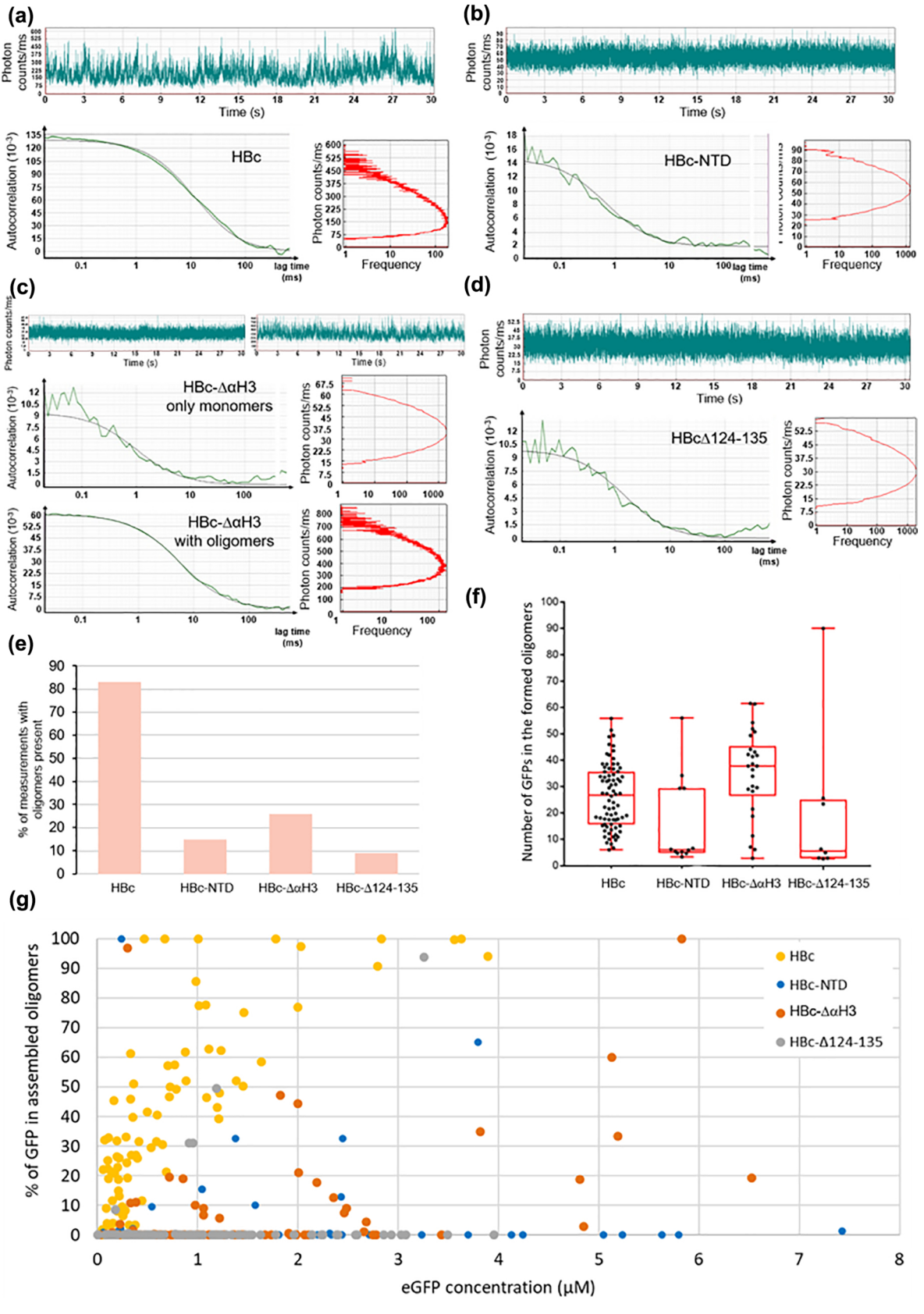
(a)
Photon counts/ms
Time (s)
Autocorrelation (10⁻³)
HBc
lag time (ms)
Photon counts/ms
Frequency
(b)
Photon counts/ms
Time (s)
Autocorrelation (10⁻³)
HBc-NTD
lag time (ms)
Frequency
(c)
Photon counts/ms
Time (s)
Autocorrelation (10⁻³)
HBc-ΔαH3
only monomers
HBc-ΔαH3
with oligomers
lag time (ms)
Photon counts/ms
Frequency
(d)
Photon counts/ms
Time (s)
Autocorrelation (10⁻³)
HBcΔ124-135
lag time (ms)
Photon counts/ms
Frequency
(e)
% of measurements with oligomers present
HBc
HBc-NTD
HBc-ΔαH3
HBc-Δ124-135
(f)
Number of GFPs in the formed oligomers
HBc
HBc-NTD
HBc-ΔαH3
HBc-Δ124-135
(g)
% of GFP in assembled oligomers
eGFP concentration (μM)
HBc
HBc-NTD
HBc-ΔαH3
HBc-Δ124-135

Figure 5

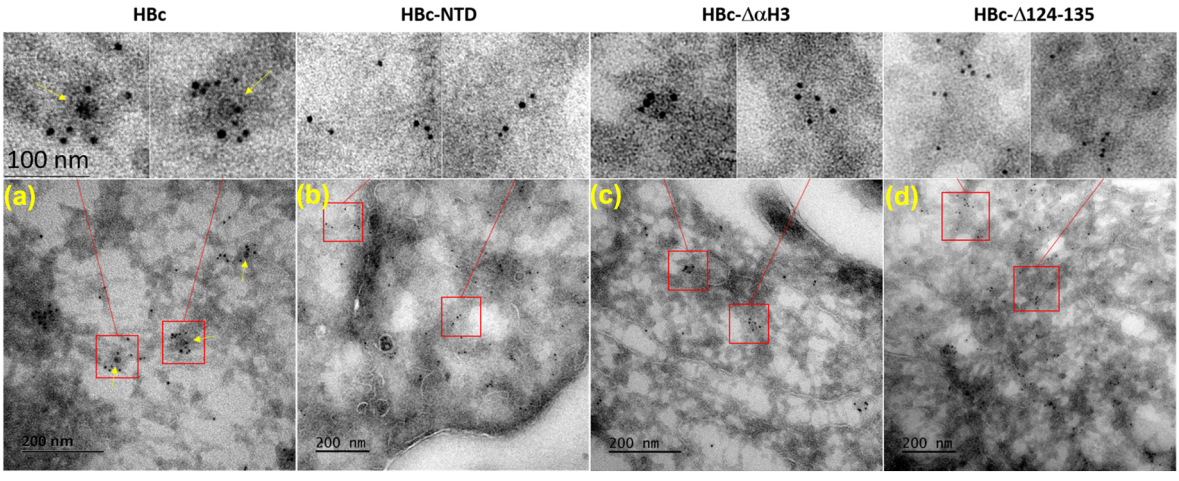
HBc
HBc-NTD
HBc-ΔαH3
HBc-Δ124-135
100 nm
(a)
(b)
(c)
(d)
200 nm
200 nm
200 nm
200 nm

Figure 6